

# A Continental Model of Curie Point Depth for China and Surroundings Based on Equivalent Source Method

Yu Lei<sup>1,2</sup>, Ligu Jiao<sup>1</sup> , Qinghua Huang<sup>2,3</sup> , and Jiyao Tu<sup>1</sup>

<sup>1</sup>Institute of Geophysics, China Earthquake Administration, Beijing, China, <sup>2</sup>Department of Geophysics, School of Earth and Space Sciences, Peking University, Beijing, China, <sup>3</sup>Hebei Hongshan National Observatory on Thick Sediments and Seismic Hazards, Peking University, Beijing, China

### Key Points:

- We inverted a new regional continental Curie Point Depth model via Equivalent Source Method
- Based on the new CPD model and measured thermal parameters, the surface heat flow and crustal temperature distribution are derived
- Our new regional CPD model exhibits better consistency with the tectonics compared to two recent global models

### Supporting Information:

Supporting Information may be found in the online version of this article.

### Correspondence to:

L. Jiao and Q. Huang,  
[lgjiao@cea-igp.ac.cn](mailto:lgjiao@cea-igp.ac.cn);  
[huangq@pku.edu.cn](mailto:huangq@pku.edu.cn)

### Citation:

Lei, Y., Jiao, L., Huang, Q., & Tu, J. (2024). A continental model of Curie Point Depth for China and surroundings based on Equivalent Source Method. *Journal of Geophysical Research: Solid Earth*, 129, e2023JB027254. <https://doi.org/10.1029/2023JB027254>

Received 8 JUN 2023  
 Accepted 27 FEB 2024

### Author Contributions:

**Conceptualization:** Ligu Jiao  
**Data curation:** Ligu Jiao  
**Formal analysis:** Yu Lei, Jiyao Tu  
**Funding acquisition:** Ligu Jiao, Qinghua Huang  
**Investigation:** Yu Lei, Ligu Jiao  
**Methodology:** Yu Lei, Jiyao Tu  
**Software:** Yu Lei  
**Supervision:** Ligu Jiao, Qinghua Huang  
**Validation:** Qinghua Huang, Jiyao Tu  
**Visualization:** Yu Lei  
**Writing – original draft:** Yu Lei  
**Writing – review & editing:** Ligu Jiao, Qinghua Huang, Jiyao Tu

**Abstract** The Curie Point Depth (CPD) marks a significant temperature boundary (~580°C) within the Earth's lithosphere. However, there has been ongoing debate regarding its spatial distribution. In this research, we utilized the Equivalent Source Method (ESM) based on Gauss-Legendre integration and data obtained from the EMM2017 model, along with a five-layer susceptibility model, to generate a 0.5° × 0.5° grid of continental CPD distribution for China and surroundings. The average CPD in the study area is 30.4 km, which is slightly shallower than the average depth of global continental Moho (~33 km). Notably, stable and cold cratonic basins, such as the Tarim Basin and the Sichuan Basin, exhibit deep CPD of ~45 km. In contrast, the North China Craton, which has experienced significant tectono-thermal activity since the Late Mesozoic, shows moderate CPD of ~30 km and a gradual uplift from west to east. The Tuva-Mongol orocline within the Central Asian Orogenic Belt, the Deccan Volcanic Province in the Indian subcontinent and the Eastern Yangtze Craton have shallow CPD of ~20 km. We estimate the surface heat flow by CPD, and the result is consistent with measurements within a RMSE of 18.1 mW/m<sup>2</sup>. When comparing the CPD with Moho, we find that the CPD may lie below Moho in stable and cold cratonic areas. In comparison to two recent global CPD models, our regional model demonstrates better alignment with tectonic features.

**Plain Language Summary** The Curie Point Depth (CPD) is the depth where crustal temperatures equal the Curie temperature of magnetite (~580°C), the dominant magnetic mineral in the crust, and hence below which there is no magnetization. It is a crucial temperature boundary within the Earth's lithosphere, providing valuable insights into the lithospheric thermal structure and dynamic evolution. Traditionally, the CPD is mostly inverted by the Power Spectral Density (PSD) method in the frequency domain, which is more suitable for shallow CPD regions. Here, we determine a new 0.5° × 0.5° continental CPD model for China and surroundings utilizing an Equivalent Source Method (ESM) in the spatial domain. Then we estimate the surface heat flow and crustal temperature with this CPD model, and discuss its relation with the Moho interface. Compared to two recent global models, our regional CPD model showcases enhanced consistency with tectonic characteristics.

## 1. Introduction

The Curie Point Depth (CPD) is the subsurface depth at which ferrimagnetic and ferromagnetic minerals become paramagnetic and suddenly lose their magnetization due to exceeding their Curie temperature (Ferré et al., 2021). The Curie temperature varies among different magnetic minerals, ranging from 150°C for Titanomagnetite (Fe<sub>2.4</sub>Ti<sub>0.6</sub>O<sub>4</sub>) to ~675°C for Hematite (α-Fe<sub>2</sub>O<sub>3</sub>) (Dunlop & Özdemir, 2007). Magnetite (Fe<sub>3</sub>O<sub>4</sub>), as the most abundant ferromagnetic mineral in the Earth's crust, has a Curie temperature of 580°C (Frost & Shive, 1986). Consequently, the CPD is conventionally assumed to be the isothermal surface at 580°C and represents the lower boundary of the magnetic layer. A reliable CPD model holds significant utility in elucidating the thermal structure of the lithosphere, reconstructing its dynamic evolution, assessing geothermal resources (Rajaram et al., 2009), and providing essential constraints for magnetic structure inversion (S. Sun et al., 2022).

Various methodologies have been devised to infer the CPD. The most straightforward way is to estimate it through surface heat flow. However, large deviations may arise due to sparse observations and uncertain underground thermal parameters. Seismic wave velocity provides an alternative way, while given that deep-seated temperature is very sensitive to the uncertainty of seismic velocity (An et al., 2015), this approach can also yield significant errors. The most commonly employed approach to estimate CPD is by inverting the Lithospheric Magnetic Field (LMF), which is generated by the induced magnetization of magnetic rocks above the CPD under

the current geomagnetic field, as well as the remanent magnetization preserved during the formation or cooling process. To obtain the LMF, the main field generated by the Earth's core, the variable field generated by spatial current systems and its induction field are subtracted from the observed total field.

The methods for estimating CPD from LMF can be broadly categorized into two types: frequency domain Power Spectral Density (PSD) method and spatial domain Equivalent Source Method (ESM). The former transforms LMF into frequency domain and determines the CPD by selecting different frequency bands and analyzing the spectral slopes (Blakely, 1995; Tanaka et al., 1999). Applications of the PSD are very extensive (e.g., Bouligand et al., 2009; Li et al., 2013; Salem et al., 2014). The latter involves subdividing the study area into grids, where each grid cell's magnetic field is approximated by an equivalent source (usually a dipole). The CPD is then obtained through forward and inverse modeling (Dyment & Arkani-Hamed, 1998; Purucker et al., 2002). The inversion workflows for these two methods are shown in Figures S1a and S1b in Supporting Information S1, respectively.

The tectonic history of mainland China is complex (Figure 1a) and the pattern of CPD variations can provide valuable information on the thermal and magnetic structure of the lithosphere. Notable examples include studies of the Tibetan Plateau (Gao et al., 2021), the Tarim Basin (Xu et al., 2021), the Songliao Basin (Wang & Li, 2018), and the Ordos Block (Gao et al., 2015). In addition to these localized investigations, regional (Xiong, Yang, Ding, & Li, 2016) and global CPD models (Li et al., 2017) have also been proposed. These studies employed the PSD method to invert the near-surface aeromagnetic data or LMF models that incorporate aeromagnetic data (e.g., EMAG2, NGDC-720). The PSD method is advantageous in fast calculation and independent of the magnetization direction, and can be used even in areas where remanent magnetization may dominate (e.g., ocean lithosphere, Li et al., 2013). However, it is based on three basic assumptions: (a) the horizontal extent of the magnetic layer is significantly greater than its thickness; (b) the magnetic source has a random or fractal distribution; (c) the direction of the radial average magnetization field and the geomagnetic field must remain constant (Demarco et al., 2020; Lin et al., 2005). Consequently, the results are sensitive to window size, wavenumber range, and fractal factor (Audet & Gosselin, 2019; Demarco et al., 2020), which can bring great uncertainties to the CPD estimation. Audet and Gosselin (2019) proposed that the PSD method is best suited for shallow CPD regions with high temperature and high heat flow, such as mid-ocean ridges.

The ESM divides the magnetic layer above the CPD into a number of tesseroids, that is, spherical prisms (or icosahedrons), and the induced field of each tesseroid is approximated by a dipole (Figure 2). ESM utilizes the high-altitude satellite field, which can better reflect large-scale and deep magnetic features compared to near surface field, especially in stable and cold cratonic areas. This method has been applied regionally in studies of the North American Craton (Purucker et al., 2002), Antarctica (Fox-Maule et al., 2005), Indian subcontinent (Rajaram et al., 2009), and Australian continent (Szwilius et al., 2022). Additionally, Fox-Maule et al. (2009) proposed a global continental CPD model concluding that the CPD in most regions are 30 ~ 50 km. Gard and Hasterok (2021) recently established another global CPD model, which claimed better agreement with continental heat flow observations. The limitations of ESM include its reliance on assumptions about induced magnetization in continental areas, the need for prior magnetic susceptibility model, and relatively slow computational speed compared to frequency domain methods. However, ESM is more suitable for larger regional scale and deep CPD inversions, such as in continental areas like mainland China, which has complex tectonic histories involving the collision and amalgamation of several Precambrian cratons (Figure 1a).

Considering the current reliance on PSD-based CPD estimations in mainland China and the complementary nature of ESM with respect to PSD, there is a need to develop a new regional CPD model based on ESM to better constrain the thermal structure at depth. In this study, three main improvements have been incorporated into the estimation of CPD in mainland China: (a) Adoption of a newly developed five-layer magnetic susceptibility model based on rock magnetism and a crustal stratification model CRUST1.0 (Laske et al., 2013, <http://igppweb.ucsd.edu/gabi/crust1.html>); (b) Utilization of an initial regional CPD model based on 3D numerical thermal structure (Y. Sun et al., 2022); (c) Application of the Gauss-Legendre integral instead of the simple dipole source approximation during the forward process. The newly determined CPD model is used to estimate the surface heat flow and crustal temperature and compared with two previous global models.

## 2. Data

To achieve a high-resolution CPD, we utilized the EMM2017 LMF model ([https://www.ngdc.noaa.gov/geomag/EMM/EMMSurveySPH\\_2017.shtml](https://www.ngdc.noaa.gov/geomag/EMM/EMMSurveySPH_2017.shtml)). The model integrates data from satellite, marine, aeromagnetic and ground

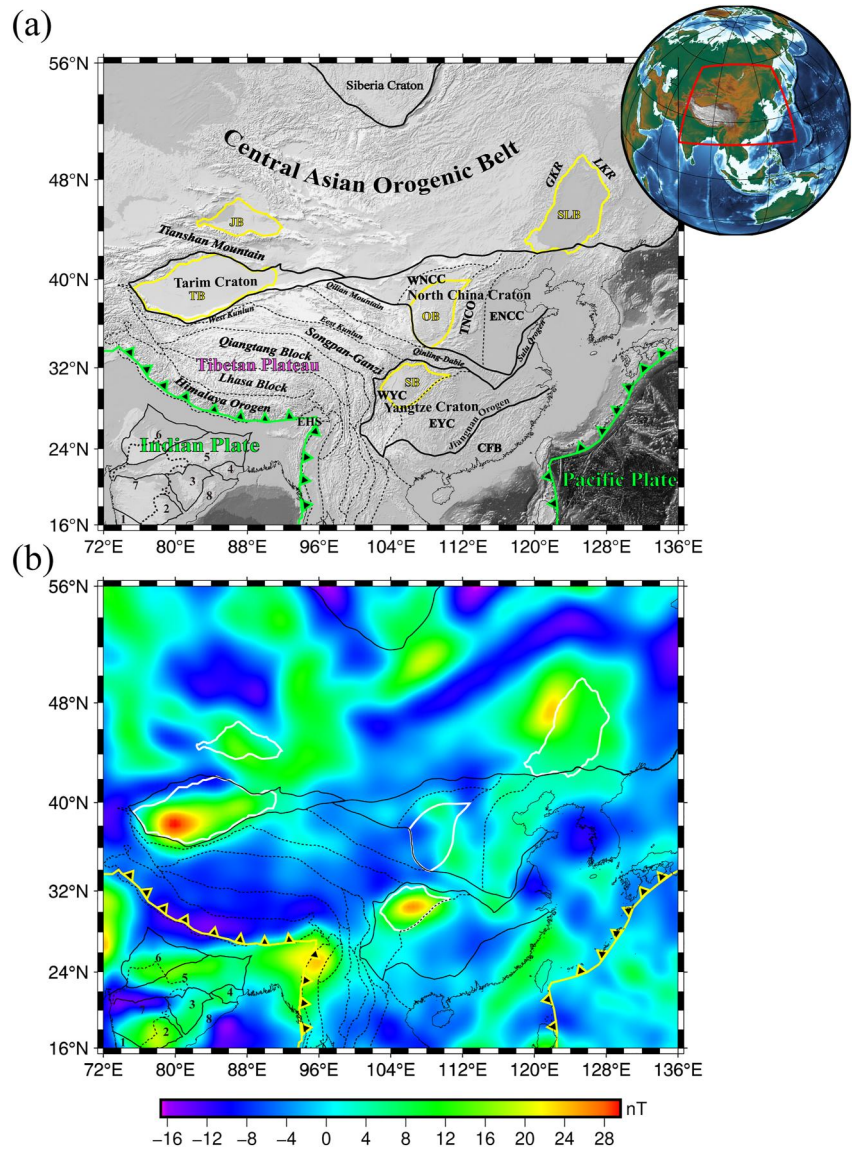


**Figure 1.** Tectonic settings and the vertical lithospheric magnetic field  $B_z$ . (a) Topography and tectonics summarized by Hasterok et al., 2022. The base map illustrates the topography provided by ETOPO1. Boundaries of plates, cratons, basins, and secondary blocks are indicated by green, black, white, and dash lines, respectively. Specific regions, such as the Tarim Basin (TB), Junggar Basin (JB), Songliao Basin (SLB), Ordos Block (OB), Sichuan Basin (SB), Western North China Craton (WNCC), Trans North China Orogen (TNCO), Eastern North China Craton (ENCC), Western Yangtze Craton (WYC), Eastern Yangtze Craton (EYC), Great Khingan Range (GKR), Lesser Khingan Range (LKR), Cathaysia Fold Belt (CFB), and Eastern Himalayan Syntaxis (EHS) are also labeled. The numbers in Indian subcontinent are 1) Western Dharwar Craton; 2) Eastern Dharwar Craton; 3) Bastar Craton; 4) Singhbhum Craton; 5) Central Indian Tectonic Zone; 6) Bundkhand Craton; 7) Deccan Volcanic Province (marked by dashed line); 8) Eastern Ghats Mobile Belt. (b)  $B_z$  at an altitude of 200 km computed using EMM2017.

magnetic surveys, with European Space Agency's SWARM satellite mission contributing to long-wavelength component and the EMAG2-v3 grid (Maus et al., 2009) contributing to short-wavelength part. It is represented by spherical harmonic expansion and has a maximum degree and order of 790, providing a higher spatial resolution (~50.6 km) compared to previous models (e.g., EMM2015, ~55.6 km). EMM2017 is a hybrid model where the main field is represented by spherical harmonics up to degree 15, while the LMF is represented by spherical harmonics from degree 16 to 790. Satellites offer high-precision vector field data, with the vertical component  $B_z$  being particularly valuable for its alignment with geological features. This component is frequently employed in magnetic studies, as highlighted in previous research (Fox-Maule et al., 2005; Kang et al., 2012;

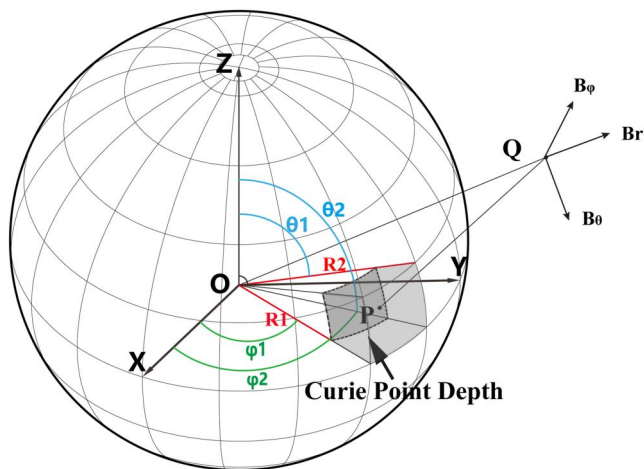


**Figure 2.** Schematic diagram of the ESM. The tesseroïd unit is represented by a gray spherical prism, with the bottom boundary representing the CPD.

Tarim Basin, Sichuan Basin, Great Khingan Range, and Eastern Himalayan Syntaxis. Moderate positive values ( $\sim 10$  nT) are identified above the Junggar Basin, Songliao Basin, North China Craton, and Indian Plate. In contrast, negative values ( $\sim -10$  nT) are evident over the Tibetan Plateau, western Tianshan, central part of Central Asian Orogenic Belt, Eastern Yangtze Craton and Cathaysia Fold Belt. In general, regions characterized by stable geological blocks exhibit remarkable positive  $B_z$ , whereas active tectonic zones display substantial negative  $B_z$ .

### 3. Method

The methodology employed to estimate CPD is illustrated in Figures S1b and S2 in Supporting Information S1. The process involves the utilization of an initial CPD model to account for the null space, which arises due to magnetic annihilators representing magnetization distributions that do not generate magnetic fields (Olsen et al., 2023). Simultaneously, the initial model provides information on the long-wavelength component of the CPD (represented by spherical harmonic degree 1–15), which is not constrained by the LMF. In this study, we utilize the CPD distribution derived from the 3D thermal structure (the 580°C isotherm in their Case C) proposed by Y. Sun et al. (2022) as the initial model (Figure S2 in Supporting Information S1). They used the latest thermal conductivity and radiogenic heat production measurements in mainland China, providing an improved regional lithospheric thermal model. Our initial CPD is thus distinct from previous studies (Fox-Maule et al., 2005, 2009; Gard & Hasterok, 2021; Rajaram et al., 2009) that relied on the Moho or 3SMAC model. The forward LMF is computed using the ESM (Section 3.3), and the CPD is iteratively updated using the conjugate gradient method (Section 3.4). The ESM relies on several premises, which will be discussed in the subsequent sections.

#### 3.1. Induced and Remanent Magnetization

The LMF is generated by the combined effects of induced magnetization and remanent magnetization from magnetic minerals located above the CPD. In oceanic lithosphere, positive and negative magnetic anomaly belts are alternately distributed, which originate from basalts in the oceanic crust formed at mid-ocean ridges during different geomagnetic polarity ages and are mainly dominated by remanent magnetization. Several remanent magnetization models for oceanic lithosphere have been established based on formation time and expansion rate (Dyment & Arkani-Hamed, 1998; Masterton et al., 2013).

In contrast, minerals in the continental lithosphere underwent complex metamorphism, remelting, and crystallization, which may result in the cancellation of remanent magnetization (Shive, 1989). Furthermore, as temperature increases, magnetic susceptibility also increases and peaks at depths close to CPD, while the remanent component attenuates rapidly (Dunlop et al., 2010; Kiss et al., 2005). Therefore, induced magnetization is generally considered to be dominant in the continental lithosphere, with its direction aligning with the main field and magnitude being proportional to the main field (Maus & Haak, 2002; Thébaud et al., 2010). In this study, we

Rajaram et al., 2009). Furthermore, the  $B_z$  at an altitude of 200 km well delineates the geological characteristics such as faults and basins, and exhibits a better correlation with seismicity than the other two components (Jiao et al., 2013; Lei et al., 2018). Hence, the  $B_z$  calculated at an altitude of 200 km from the EMM2017 model is used (the effects of the other two components are discussed in Supplementary Information) to invert the CPD.  $B_z$  is computed by:

$$B_z = -B_r$$

$$= - \sum_{n=16}^{790} \sum_{m=0}^{m=n} (n+1) \left(\frac{a}{r}\right)^{n+2} (g_n^m \cos m\varphi + h_n^m \sin m\varphi) P_n^m(\cos \theta) \quad (1)$$

where  $n$  and  $m$  are spherical harmonic degree and order, respectively,  $a$  is the earth's reference radius, and  $(r, \theta, \varphi)$  is the coordinates of field point (Figure 2).

The resulting vertical anomaly ( $B_z$ ) map at 200 km altitude is shown in Figure 1b. Significant positive  $B_z$  values ( $>20$  nT) are observed above the

**Table 1**  
*Magnetic Susceptibility Model Used for CPD Inversion*

	SiO <sub>2</sub> content/%	Minerals	Representative magnetic lithology	Magnetic susceptibility/SI
Sediment	~65	quartz, feldspar, calcite	Sedimentary rock	0
Upper crust	~65	quartz, feldspar, biotite	Granite	0.01
Middle crust	~62	quartz, feldspar, biotite, amphibole	Syenite	0.04
Lower crust	50–66	quartz, feldspar, biotite, amphibole, pyroxene, olivine	Lower crustal Peridotite	0.08
Lithospheric mantle	41–45	olivine, pyroxene, feldspar	Unaltered ultramafic rock	0.001 <sup>a</sup>

<sup>a</sup>Remain controversial, check the text for details.

only consider induced magnetization in continental regions, while both induced and remanent components in oceanic areas. We use the global oceanic remanent magnetization model established by Masterton et al. (2013). Based on this model, the remanent part above degree 16 (Figure S3 in Supporting Information S1) has been removed from the EMM2017 model. In terrestrial areas where remanence could dominate, such as volcanic regions, the results obtained through ESD might be unreasonable (Fox-Maule et al., 2009). Careful consideration is required when conducting geological interpretations in such cases.

### 3.2. Susceptibility Model

To perform CPD inversion based on ESD, a prior information about the susceptibility of the Earth's crust is necessary. Traditionally, a simplified susceptibility model has been used, assuming a uniform magnetization for both oceanic and continental crust (Fox-Maule et al., 2005; Purucker et al., 2002; Rajaram et al., 2009), which oversimplifies the real geological conditions. Recent ESD-based inversion (Gard & Hasterok, 2021) has employed a global Vertically Integrated Susceptibility (VIS) model (Hemant & Maus, 2005), which is constructed based on sampling of rock magnetization, geological types, and seismic velocity structure. However, the susceptibility is strongly coupled with the CPD depth, leaving it difficult to separate the CPD contribution.

Despite extensive measurements and statistical work on rock magnetism (Hunt et al., 1995; Xiong, Yang, Ding, Li, et al., 2016), the distribution of measurements is extremely uneven, and there are only a few drilling data and the drilling depth is quite limited. Specifically, for the same rock type, the range of susceptibility can vary widely. As a result, there is currently no available regional pure lithospheric susceptibility model. To estimate the CPD, we propose a layered susceptibility model based on rock magnetism and the crustal model - CRUST1.0, as listed in Table 1. Referring to CRUST1.0, the continental lithosphere is divided into five layers, including the sedimentary layer, the upper, middle, and lower crust, and the lithospheric mantle. The lithologies can be classified into acidic, neutral, basic, and ultrabasic categories based on their SiO<sub>2</sub> content, roughly corresponding to the upper, middle, lower crust, and lithospheric mantle, respectively. Minerals in each layer are assigned according to Sen (2014) and Haldar (2020). Since the magnetization of sedimentary rocks is generally negligible compared to igneous rocks, the susceptibility is set to zero. Referring to the susceptibility of the lithologies in China summarized by Xiong, Yang, Ding, Li, et al. (2016), the representative magnetic lithologies of the three crustal layers are set to granite (~0.01 SI), syenite (~0.04 SI) and lower crustal peridotite (~0.08 SI), respectively.

The magnetism of lithospheric mantle remains controversial. Although measurements (Xiong, Yang, Ding, Li, et al., 2016) show that the ultramafic rocks in the lithosphere mantle have a high susceptibility (~0.057 SI), it may be the result of alteration (such as serpentinization) or contamination after entering the crust, and cannot represent the true susceptibility of the lithosphere mantle. Early studies of mantle xenoliths and exposed sections of the mantle and lower crust had concluded that magnetite was absent from the mantle (Wasilewski & Mayhew, 1992). However, recent measurements on fresh and unaltered mantle xenoliths demonstrate that they regularly contain magnetite, and the concentrations may range from a few ppm to a maximum of ~3,500 ppm. These fresh mantle xenoliths show low susceptibility ( $10^{-4} \sim 10^{-2}$  SI) (Ferré et al., 2021). Here we set the susceptibility in lithospheric mantle to  $10^{-3}$  SI.

### 3.3. Forward ESM Scheme

The magnetic shell situated above the CPD can be divided into spherical prisms along latitudes and longitudes, also known as tesseroids (Figure 2). Former studies (Gard & Hasterok, 2021; Rajaram et al., 2009) calculated the LMF at altitudes of 300 or 400 km, approximating each tesseroid by a dipole. At an altitude of 200 km or lower, a more precise calculation will be advisable. As there is no analytical expression, the Gauss-Legendre numerical integration (Asgharzadeh et al., 2008) with  $4 \times 4 \times 4$  nodes in each tesseroid is used. Formulas of the forward scheme are included in Supplementary Information.

The study area (N16°-N56°, E72°-E136°) is divided into tesseroids with individual lateral dimensions of  $0.5^\circ \times 0.5^\circ$ , according to the resolution of EMM2017. Vertically, we subdivide the grids based on the layered susceptibility model outlined in Table 1. The inducing field is derived from the IGRF13 model (Alken et al., 2021). As the EMM2017 model does not encompass the long-wavelength LMF components for  $n = 1 \sim 15$ , a High-Pass (HP in Figure S1b in Supporting Information S1) spherical harmonic filter is applied during each iteration, retaining only the short-wavelength parts for  $n \geq 16$ .

### 3.4. Li-Oldenburg Regularization Inversion

In the inversion process, we adopt the scheme developed by Li and Oldenburg (1996). The objective function designed by them is:

$$\Phi = \Phi_d + \mu\Phi_m + \lambda\Phi_b, \quad (2)$$

where  $\Phi_d$  is the data misfit function,  $\Phi_m$  is the model objective function,  $\Phi_b$  is the logarithmic barrier function,  $\mu$  is the regularization parameter,  $\lambda$  is the barrier parameter.  $\Phi_d$  is defined by:

$$\Phi_d = \|\mathbf{W}_d(d^{obs} - \mathbf{G}m)\|^2 \quad (3)$$

where the matrix  $\mathbf{W}_d$  is a diagonal matrix related to the observational errors in the data,  $\mathbf{G}$  is the sensitivity kernel matrix determined by the aforementioned forward modeling process,  $d^{obs}$  is the LMF ( $B_z$ ), and  $m$  is the model parameter to be solved, namely the CPD.  $\Phi_m$  is defined by:

$$\Phi_m = \|\mathbf{W}_m(m - m_{ref})\|^2 \quad (4)$$

where  $\mathbf{W}_m$  is the weighting matrix,  $m_{ref}$  is the reference CPD model which is assumed to be constant and set to zero in this study. To confine the CPD within a reasonable range, a logarithmic barrier function (Li & Oldenburg, 2003) is incorporated into the total objective function, which is defined as:

$$\Phi_b = -2 \sum_{i=1}^M \left( \ln \frac{m_i - b_i^{low}}{b_i^{up} - b_i^{low}} + \ln \frac{b_i^{up} - m_i}{b_i^{up} - b_i^{low}} \right) \quad (5)$$

where  $M$  is the total number of model units,  $b_i^{low}$  is the lower limit of the  $i$ th model, and  $b_i^{up}$  is the upper limit of the  $i$ th model. When the value of  $m_i$  approaches the limits, the logarithmic barrier function will approach infinity, ensuring that the model is kept within the appropriate range. Based on previous CPD studies, we set the lower and upper limits as 0 and 70 km, respectively.

The CPD model is updated iteratively based on the difference between calculated  $B_z$  and observed  $B_z$  (EMM2017) until the update is sufficiently small (mean  $|\Delta m| < 0.15$  km), at which point the final CPD model is output (Figure S1b in Supporting Information S1). Details of the differences between calculating processes of this study and Gard and Hasterok (2021) (GH21) are shown in Table 2.

**Table 2**  
Comparisons of CPD Calculating Processes Between GH21 and This Study

Difference/model	GH21	This study
Data	Three components from LCS-1 with $n = 16-100$ at 300 km altitude	Bz component from EMM2017 with $n = 16-790$ at 200 km altitude
Forward scheme	Dipole as equivalent source	G-L integration of Tesseroid
Initial CPD model	Hybrid thermal model with TC1 and 3SMAC	Thermal model from Y. Sun et al. (2022)
Susceptibility model	Vertical Integrated Susceptibility (Hemant & Maus, 2005)	Five-layer susceptibility proposed by this study
Remanent magnetization model	Dyment and Arkani-Hamed (1998) and Purucker and Dyment (2000)	Masterton et al. (2013)
CPD constraint	No constraint	Constraint between 0 and 70 km

## 4. Results

Figure 3 presents our novel CPD distribution, while Figure 4 illustrates the statistical features of various typical tectonic blocks. Generally, there is a positive correlation between CPD and  $B_z$ , where stronger positive  $B_z$  corresponds to deeper CPD. However, the CPD pattern shifts northward compared to  $B_z$ , similar to the reduction-to-the-pole (RTP) results of LMF at middle and low latitudes in the northern hemisphere. This offset could be ascribed to the tilted magnetized induced by the main field. The CPD ranges from 16 to 52 km within the study area, with an average depth of 30.4 km, which is slightly shallower than the global average continental Moho (~33 km). In general, the CPD of stable cratons (e.g., Tarim Craton, ~50 km), Craton basins (Sichuan Basin, ~45 km) or cratonic foreland basins (Junggar Basin, ~45 km) is deep, while the CPD of active orogenic belts (e.g., Tuva-Mongol orocline, ~15 km) or suture belts (South Tianshan-Beishan-Solonker, ~25 km, Jiangnan Orogen, ~20 km) is shallow.

The average CPD of the Tibetan Plateau is 31.2 km (Figure 4d), close to the overall average of the study area. Deep CPD (~40 km) exists in the Western and Eastern Himalayan Syntaxis areas bordering the Indian Plate in the south and the Qaidam Basin in the north, while shallow CPD (~25 km) shows in northwest Tibetan Plateau. The Indian Plate is composed of several micro-cratonic blocks (Figure 1a), including Dharwar and Bastar. Moderate-deep CPD (30~40 km) appears in these cratonic blocks, while noticeable shallow CPD (~20 km) exists both in and to the west of the Deccan Volcanic Provinces, which is the Earth's largest continental flood basalt provinces.

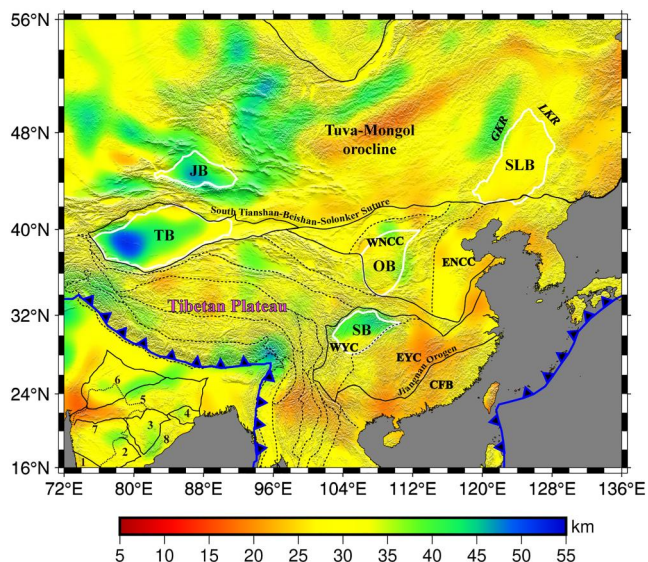


**Figure 3.** The new continental CPD model estimated in this study. Tectonic boundaries and labels are the same as Figure 1.

## 5. Discussion

### 5.1. CPD and Geological Structure

The CPD obtained in this study shows a good match with the geological structure. In the old and stable cratonic regions, the CPD is usually deep. However, in regions that have experienced significant tectono-thermal events since Mesozoic and Cenozoic, the CPD uplifts obviously. In the western part of the study area, the CPD of the Junggar Basin, the Tarim Basin, and some parts of the Indian Plate is deep, while the CPD of the Deccan Volcanic Provinces formed since Late Cretaceous and the inner Tibetan Plateau affected extensively by the India-Asia collision since Cenozoic is shallow. In the eastern part, influenced by the subduction and dehydration of the western Pacific Plate in Mesozoic and Cenozoic, the continental CPD is generally shallow, and gradually deepen to the west. As a back-arc extensional basin, the mean CPD of Songliao Basin is only 27.9 km (Figure 4c). While the CPD of Great Khingan Range, to the west of the Songliao Basin, is as deep as 40 km, which is consistent with the cold and ancient lithospheric basement (Jia et al., 2022). The North China Craton, one of the pre-Cambrian cratons,

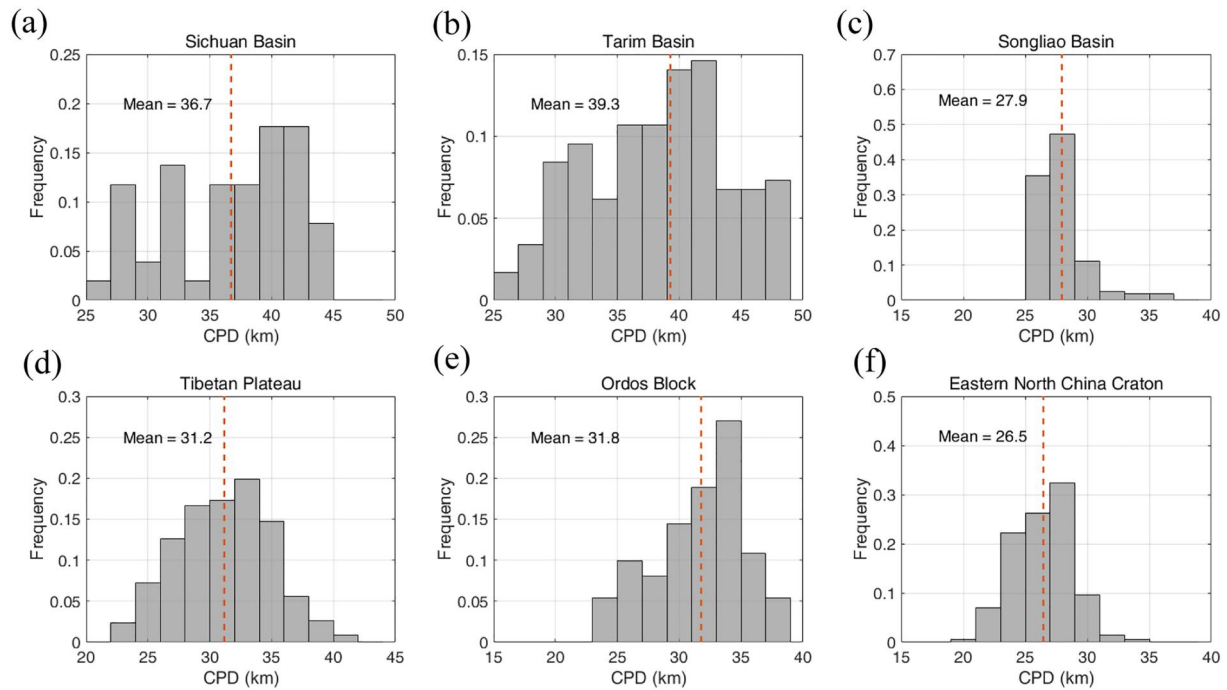


**Figure 4.** Statistical characteristics of CPD across various tectonic blocks. Red dash line marks the mean value for each region.

has a mean CPD of only 26.5 km in its eastern part (Figure 4f), which is even shallower than the continental average (30.4 km) of China and surroundings. By contrast, the mean CPD of Western North China Craton is 31.8 km (Figure 4e). These reflect well the thermal impacts of North China Craton destruction (He, 2015; Li et al., 2015; Zhu et al., 2012). Relative to the deep CPD of Western Yangtze Craton (especially the Sichuan Basin), the CPD of Eastern Yangtze Craton and Cathaysia Fold Belt is as shallow as ~20 km.

## 5.2. CPD and Surface Heat Flow

Since the CPD represents the depth to the isotherm of 580°C, a reasonable CPD model should be roughly consistent with surface heat flow observations, although they may be disturbed by local thermal conditions. Here, we compared our CPD model with the corrected heat flow measurements in mainland China provided by Jiang et al. (2019), which include Class A to C data at 1,136 locations. Class D measurements are excluded due to strong influence of deep geothermal fluids or near surface factors. As is shown in Figure 5a, the heat flows of Tarim Basin and Junggar Basin (with deep CPD) are below 60 mW/m<sup>2</sup>, and some values are even below 40 mW/m<sup>2</sup> (called ‘cold basin’ by Jiang et al., 2019). In the Qaidam Basin and Sichuan Basin (with relative deep CPD), most of the heat flows are 40~60 mW/m<sup>2</sup>, some are 60~80 mW/m<sup>2</sup>, and only a few are below 40 mW/m<sup>2</sup> (‘warm basin’). Most of the heat flow in the Ordos Basin (with moderate and relative deep CPD, ‘warm basin’) is 60~80 mW/m<sup>2</sup>, and most of the heat flow in its western margin is 40~60 mW/m<sup>2</sup>. Compared with basins above, the heat flows in the Songliao Basin (with moderate and shallow CPD) are significantly higher, ranging from 40 to 100 mW/m<sup>2</sup> (‘hot basin’). For the eastern China, the heat flows gradually drop to the west, which is in accord with the depression of CPD. Heat flows below 40 mW/m<sup>2</sup> spread mainly along the eastern edge of Trans North China Orogen (TNCO). The heat flows in southeast China are a little more complicated in that they rise first and then decrease to the west, which is also in line with the change of the CPD that uplifts first and then depresses.

For further comparison, we calculated the theoretical heat flows based on 1D steady-state heat conduction equation via CPD (the derivation process is outlined in Supplementary Information):

$$q_s = k \frac{T_c - T_0}{Z_c - Z_0} + \delta^2 H_0 \frac{e^{-Z_c/\delta} - e^{-Z_0/\delta}}{Z_c - Z_0} + \delta H_0 e^{-Z_0/\delta} \quad (6)$$

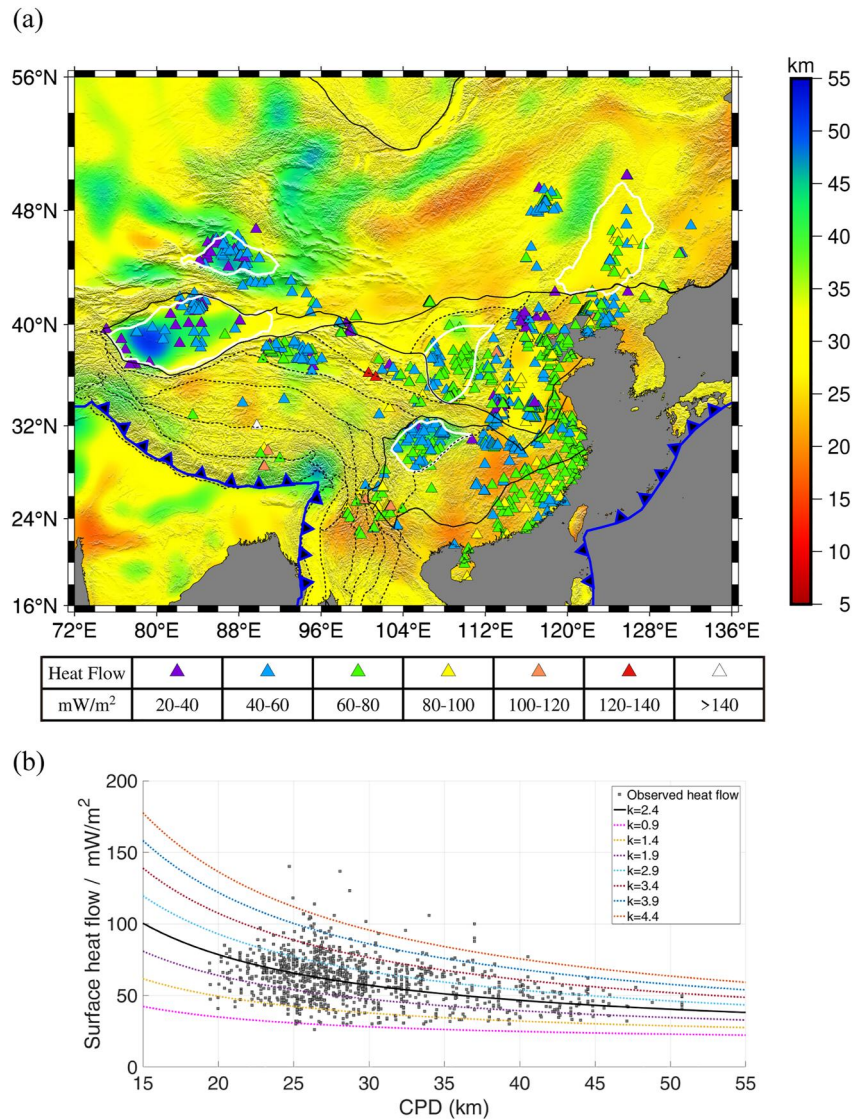


**Figure 5.** Comparison between CPD and surface heat flows. (a) Direct comparison. Heat flows are corrected measurements in mainland China provided by Jiang et al. (2019), which include Class A to C data at 1,136 locations and marked by triangles with different colors. (b) Observed and calculated heat flows. Gray squares are observations. Dashed lines with different colors represent calculated values by CPD, using varied thermal conductivities, constant heat production rate, and fixed decay distance of radioactive heat production. Black solid line marks the best fit conductivity.

where  $k$  is the thermal conductivity,  $H_0$  is the mean surficial radioactive heat production rate (set to  $1.56 \mu\text{W}/\text{m}^3$ ),  $T_0$  is the surface temperature ( $0^\circ\text{C}$ ),  $T_c$  is the Curie temperature ( $580^\circ\text{C}$ ),  $Z_0$  is the surface elevation,  $Z_c$  is the CPD, and  $\delta$  is the decay distance of radioactive heat production (set to 10 km). The comparison of the two is shown in Figure 5b. It's noticeable that the majority of observations fall within the estimated heat flow curves generated by varying conductivities ( $k = 0.9\sim 4.4 \text{ W}/(\text{m}^\circ\text{C})$ ). The fitted conductivity is  $2.4 \text{ W}/(\text{m}^\circ\text{C})$ , close to the typical value of granite. As the CPD depresses, the estimated heat flow curves gradually narrow, and the estimations align more closely with observations, indicating that estimations in deep CPD regions may be closer to observations. The correlation coefficient between observations and estimations is  $-0.35$ , indicating a weak negative correlation.

For more exact estimation, we incorporate the observed conductivity and radiogenic heat production data and take into account the variation of conductivity with depth. The 1D steady-state heat conduction equation is written as:

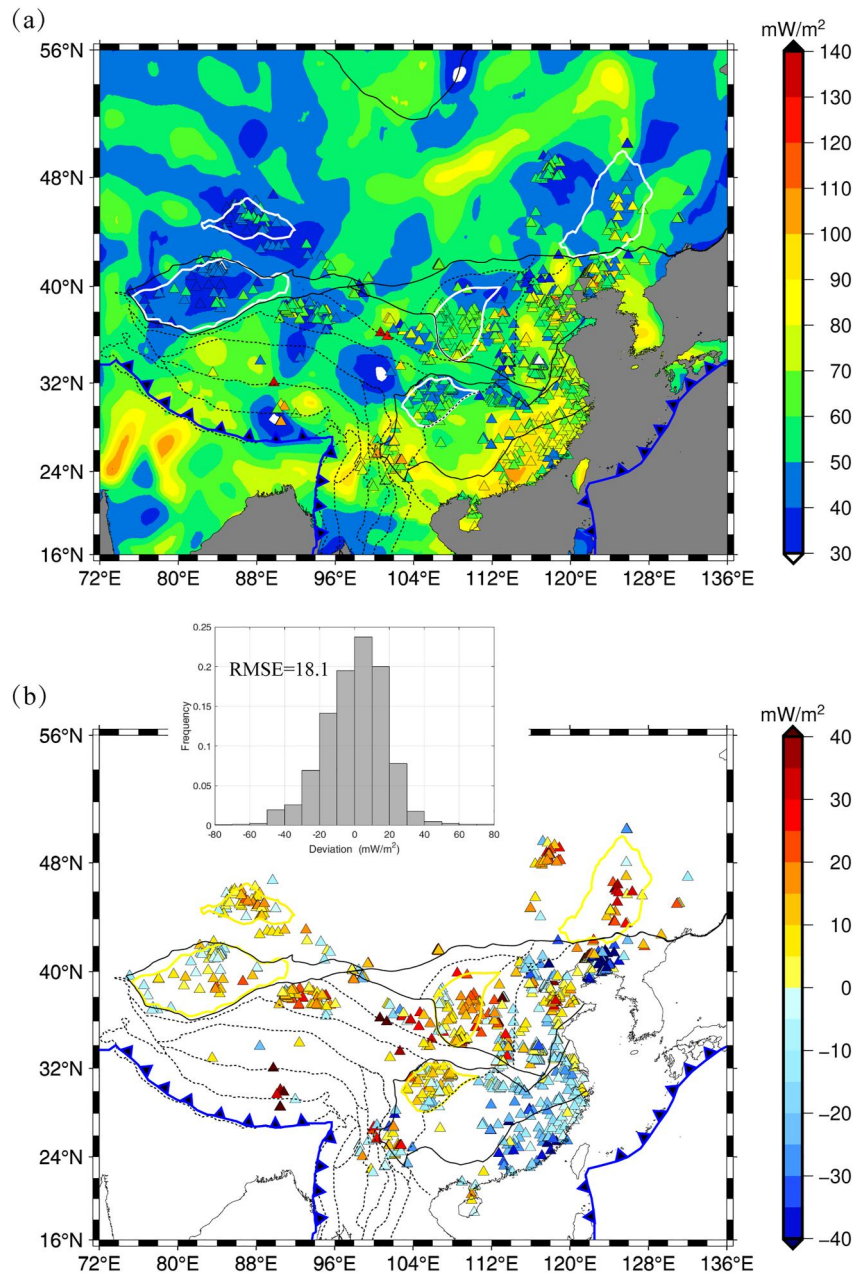


**Figure 6.** Comparison between observed and estimated heat flows, incorporating measured thermal conductivity and radiogenic heat production data. (a) Observed (colored triangles) and estimated heat flows. (b) Observed - estimated heat flows. The statistical characteristic is shown in the histogram.

$$\frac{\partial}{\partial z} \left[ k(T, z) \frac{dT}{dz} \right] = -H_0 e^{-z/\delta} \quad (7)$$

We select the vertically varied conductivity model summarized by Y. Sun et al. (2022):

$$k = \begin{cases} k_0(1 + cz)/[1 + b(T - 293.15)], & \text{for crust} \\ k_0 [1.23 \times 10^{-10} \times 1/0.518 + 7.89 \times 10^{-4}T], & \text{for mantle} \end{cases} \quad (8)$$

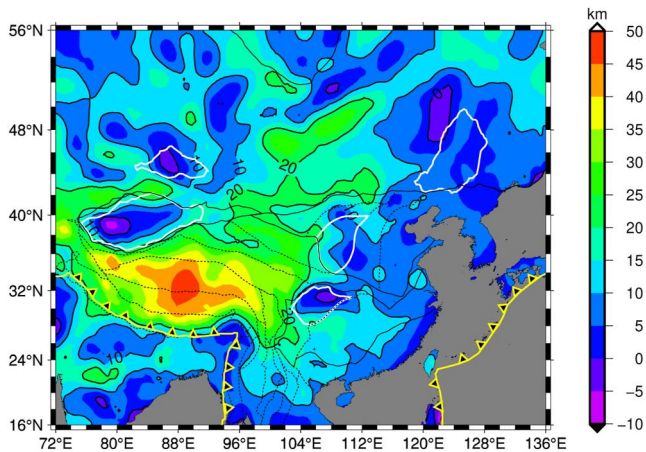


**Figure 7.** Difference between the CPD and Moho depth (CRUST1.0). Positive value indicates that the Moho is deeper than CPD.

differences fall within  $\pm 40$  mW/m<sup>2</sup>, with an RMSE of 18.1 mW/m<sup>2</sup>. Considering the observed error is  $\sim 20$  mW/m<sup>2</sup> (Jiang et al., 2019), it suggests that the CPD model developed in this study can effectively constrain the thermal state, particularly in regions without direct measurements. The discrepancies could be due to sparse data on conductivity and radiogenic heat production, lower-quality heat flow observations, or the fact that these regions (e.g., the Tibetan Plateau) may not fully satisfy steady-state heat conduction conditions (Y. Sun et al., 2022).

### 5.3. CPD and Moho

Early studies equated the Moho with the CPD, as no magnetite was found in xenolith samples sourced from the mantle (Wasilewski & Mayhew, 1992). However, subsequent studies (e.g., Blakely et al., 2005; Ferré et al., 2013; Williams & Gubbins, 2019) proposed that the long-wavelength LMF most likely have mantle origins. Furthermore, recent measurements on fresh mantle xenoliths demonstrated that they regularly contain magnetite, which provides carrier for mantle magnetic anomaly (Ferré et al., 2021). Laboratory high-temperature and high-pressure experiments (Kupenko et al., 2019) also indicated that some Fe-oxides, such as hematite, remain magnetic in the upper mantle at depth of  $\sim 600$  km, thereby contributing to the long-wavelength LMF. Mantle contributions to LMF would be, however, limited to specific regions of cold temperatures (such as ancient cratons and subducting slabs) and areas where the upper mantle has been substantially hydrated (Ferré et al., 2021; McEnroe et al., 2017).

To check whether and where the lithospheric mantle is magnetized, our CPD model is compared with the interpolated CRUST1.0 model. The discrepancies between them are illustrated in Figure 7. For most of the study area, the CPD lies shallower than Moho. This is notably pronounced in the western China, including the Western Tianshan, Tibetan Plateau and central of Central Asian Orogenic Belt (CAOB), where the CPD is significantly shallower than the Moho (by  $> 20$  km). These imply a thermally active upper-to-middle crust. In contrast, most of the eastern China exhibits a much closer proximity between CPD and Moho, with a difference  $< 10$  km. Given the inherent uncertainties in inversion, it is conceivable that these two interfaces partially overlap. It can be hypothesized that the Moho temperature in these regions approximates 580°C.

In regions such as the central Junggar Basin, western Tarim Basin, northern Sichuan Basin and Great Khingan Range, the CPD may reside beneath Moho. This suggests that these areas possess a relatively cold upper mantle, which could lead to a relative stable, strong lithosphere and low surface heat flow. Our study thus supports Ferré et al. (2021)'s viewpoint that the uppermost mantle is magnetized in ancient and stable cratons.

### 5.4. Comparison Between Different CPD Models

Previous studies have inverted global CPD models by using ESD and PSD respectively. Here we select two recent inversions to compare with this study. The two global CPD models are shown in Figure 8, where Figure 8a is the ESD result presented by Gard and Hasterok (2021, GH21), and Figure 8b is the PSD result presented by Li

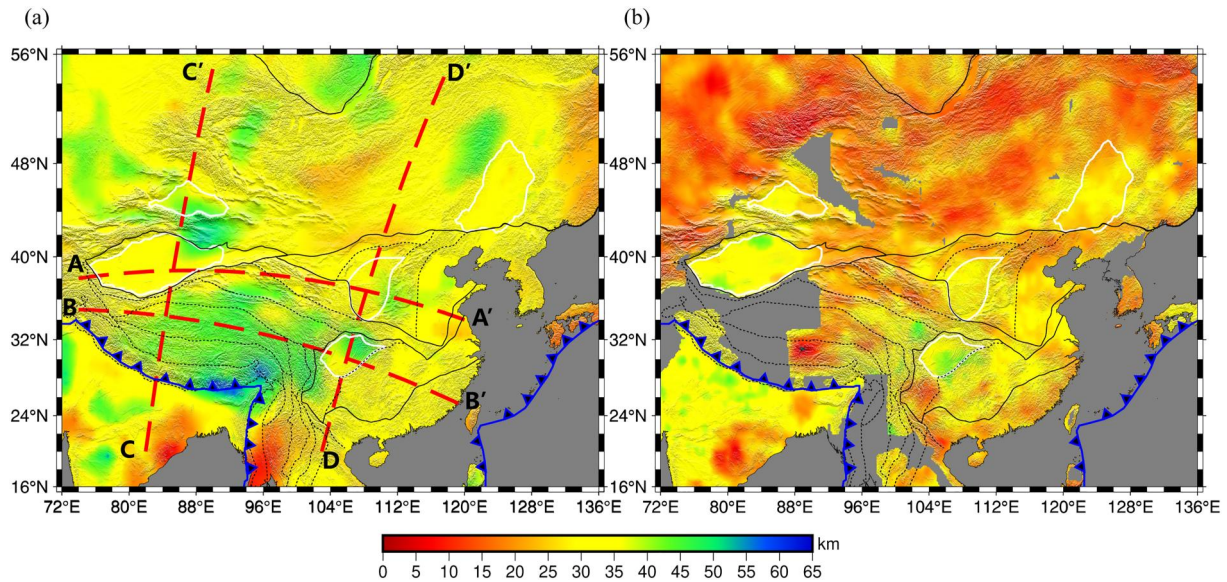


**Figure 8.** Two global CPD models in the study area. (a) Gard & Hasterok, 2021; (b) Li et al., 2017. Red dash lines denote profiles showed in Figures 9 and 10.

et al. (2017, L17). The grid resolution is  $1^\circ \times 1^\circ$  and  $0.17^\circ \times 0.17^\circ$  respectively, and both models are interpolated into grids of  $0.5^\circ \times 0.5^\circ$ .

The CPD distribution of the GH21 model in eastern China is relatively similar to the result of this study, but in EYC and CFB, the CPD is uniformly distributed at depth of  $\sim 30$  km, which is in contrast to our shallower and fluctuated CPD pattern. In western China, the contrast is even stronger, especially in the Tarim Craton and Tibetan Plateau. The GH21 model has a uniform and relative deep CPD ( $\sim 35$  km) distribution in the Tarim Craton and a uniform and deep CPD ( $\sim 45$  km) distribution in the Tibetan Plateau. The CPD of this study shows more spatial variation characteristics, with deep CPD ( $\sim 50$  km) in western Tarim, moderate CPD ( $\sim 30$  km) in central Tibet, and shallow CPD ( $< 25$  km) in northwest Tibet. Compared with these two ESD models, the overall CPD of L17 model is relatively shallow, and it does not give obvious deep CPD distribution in the Greater Khingan Range, Ordos Basin and Junggar Basin. The deep CPD of Tarim Basin is distributed in the north and southwest, and an overall shallow CPD is displayed in the eastern Tibetan Plateau, while the CPD in western Tibet is missing.

For more detailed comparison, we select 4 profiles, whose positions are shown in Figure 8a, and the results are shown in Figure 9. The heat flows are calculated by the same parameters as those for Figure 6a. From the latitude profile AA' (Figure 9a), the CPD of this study is significantly deeper than the other two models in western Tarim, and the calculated heat flow is in good agreement with the measured one. Furthermore, our CPD is deeper than the Moho here. In eastern Tarim, our CPD gradually uplifts above the Moho and gets close to the other two models, and the calculated heat flow is significantly lower than the measurement. From Qilian Mountain to Eastern North China Craton (ENCC), our CPD curve varies basically between the other two model curves. The calculated heat flow in OB and ENCC is matched well with the measurement, but is lower than the measurement in western Qilian and TNCO.

From the latitude profile BB' (Figure 9b), the CPD of this study is significantly shallower (by  $\sim 15$  km) than GH21 model and also significantly shallower (by  $\sim 40$  km) than the Moho in Tibetan Plateau. In eastern Tibet, the CPD of this study is similar to that of the L17 model (the CPD of L17 is missing in western Tibet). Since there is only one heat flow measurement here, it is impossible to determine which model is better via heat flow. While, seismic and magnetotelluric studies reveal that low velocity and high conductivity anomalies are widespread in the mid-lower crust of Tibet (Li et al., 2012; Rippe & Unsworth, 2010; Tan et al., 2023). Additionally, evidence of ultra-high temperature metamorphic events at  $1,100\text{--}1,150^\circ\text{C}$  under pressure of  $0.8\text{--}0.9$  GPa has been found in northern Tibet (Zhang et al., 2022). All these suggest that the middle and lower crust of Tibet is hot, which is corresponding to shallow CPD and consistent with our model. From the eastern part of

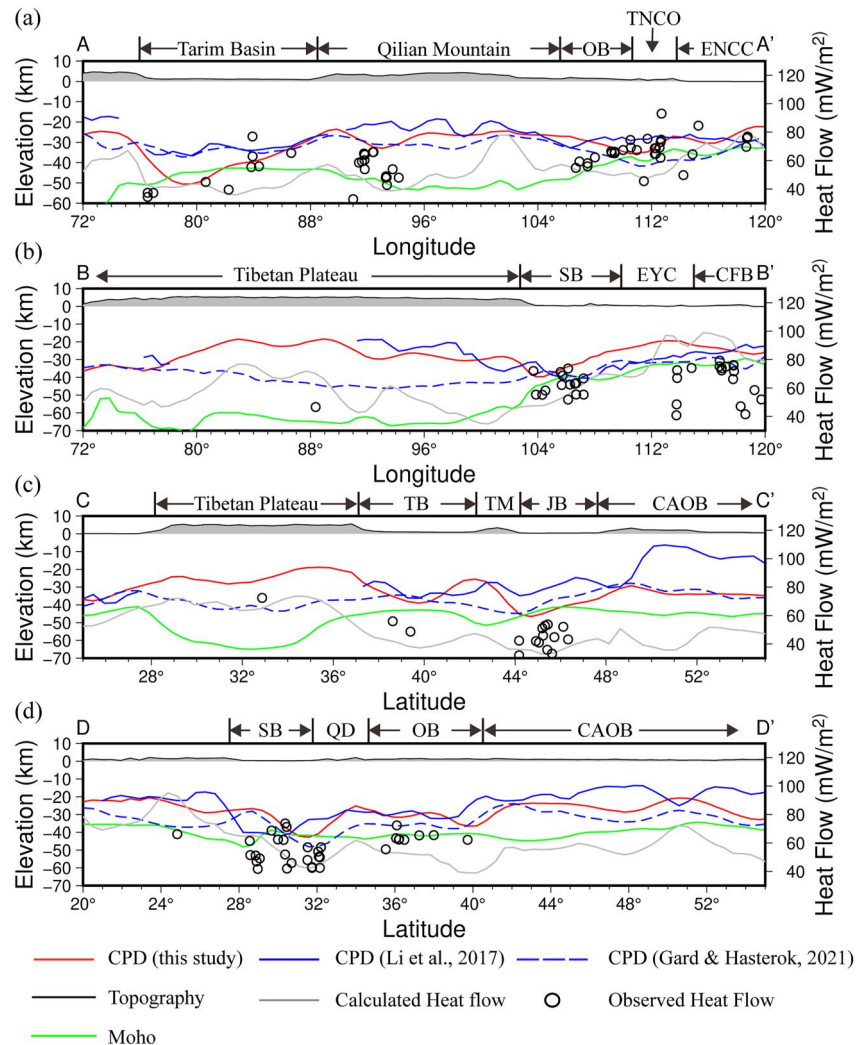


**Figure 9.** Profiles showing comparisons between various CPD models, Moho and heat flows. Check Figure 8 for profile locations.

BB', the three models are close, and the CPD of this study is slightly shallower (by ~10 km) than the other two. In Sichuan Basin, the calculated heat flow is in good agreement with the observation, while in Eastern Yangtze Craton and Cathaysia Fold Belt, the calculated value is significantly higher. The CPD here is above (by ~10 km) and close to the Moho.

From the meridian profile CC', the CPD in this study is significantly shallower (by ~15 km) than GH21 model in Tibetan Plateau, and our CPD shows obvious variation with different tectonic attributes. In orogenic belts such as Tibetan Plateau, Tianshan Mountain and CAOB, the CPD uplifts, while in craton basins like Tarim Basin and Junggar Basin, the CPD depresses. The GH21 model does not show such obvious variations, and its varying tendency is exactly the opposite of our model. The calculated heat flow matches well with the measurement. The CPD of this study is shallower than the Moho as a whole, but close to Moho in Tarim Basin and slightly deeper than Moho in southern Junggar Basin. The L17 model in Tarim Basin, Tianshan Mountain and Junggar Basin is similar to this study, but significantly shallower (by ~20 km) in CAOB.

From the meridian profile DD', the three models are close, and the CPD curve of this model lies roughly between those of the other two models. The CPD is ~10 km above Moho. The calculated heat flow matches the measurement well, while at Ordos Block, the calculated one is slightly lower (by ~10 mW/m<sup>2</sup>). For reference, the calculated crustal temperature profiles based on the CPD of this study are presented in Figure 10. As can be seen,

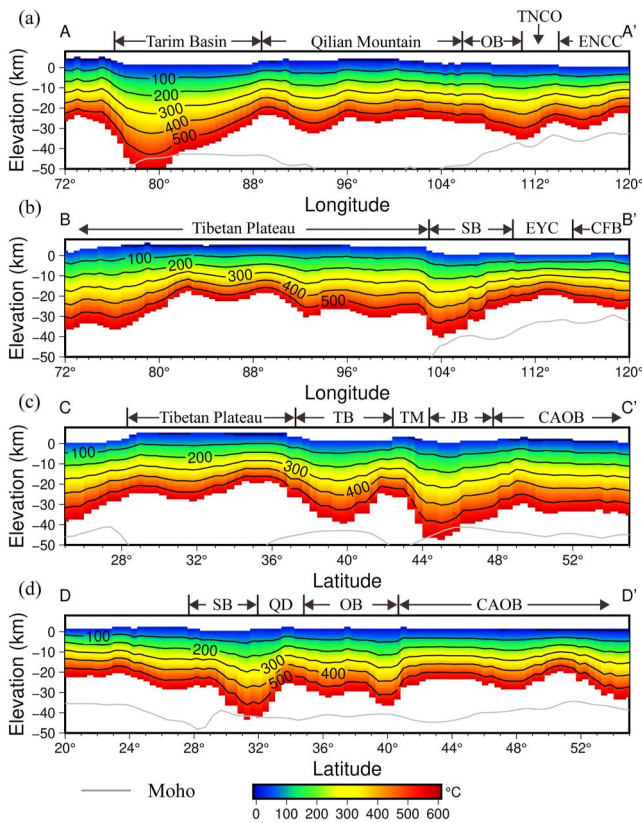


**Figure 10.** Crustal temperature profiles based on CPD. Thermal parameters are the same as those of Figure 6. Check Figure 8 for profile locations.

the Tibetan Plateau, Tianshan Mountain, CAOB regions have hotter middle and upper crust temperatures, while the Tarim Basin, Junggar Basin and Sichuan Basin regions have colder lower crust temperatures.

### 5.5. Uncertainty Analysis

Factors affecting the reliability of CPD inversion include errors in the employed LMF model, the induction assumption, the initial model and the magnetization model. Discussions on the first three can be found in Supplementary Information. Here, we focus on the influence of the magnetization model. Two different models are set and compared with the model used in this study. The susceptibility model parameters and CPD differences are shown in Figure 11. The CPD differences caused by different susceptibility models in most study areas are less than 4 km. Lower susceptibility results in more drastic CPD fluctuation (Figure 11a), that is, the CPD in deep CPD region is deeper, and that in shallow CPD region is shallower. By the same way, a higher susceptibility model results in gentler CPD variation (Figure 11b). For local susceptibility variation, since the CPD and susceptibility change roughly reverse, and the calculated heat flow and CPD change roughly reverse, the heat flow and susceptibility change roughly in the same trend. Where the heat flow calculated by CPD is higher than the measurement, it is possible that the model susceptibility is higher than the actual value, and vice versa.

### 6. Conclusions

In this investigation, the  $B_z$  component of LMF obtained from the EMM2017 model at an altitude of 200 km is utilized to invert a  $0.5^\circ \times 0.5^\circ$  CPD distribution in mainland China and adjacent tectonic plates via ESM. In the forward process, we use G-L numerical integration instead of simple dipole source approximation. In addition, a susceptibility stratification model is

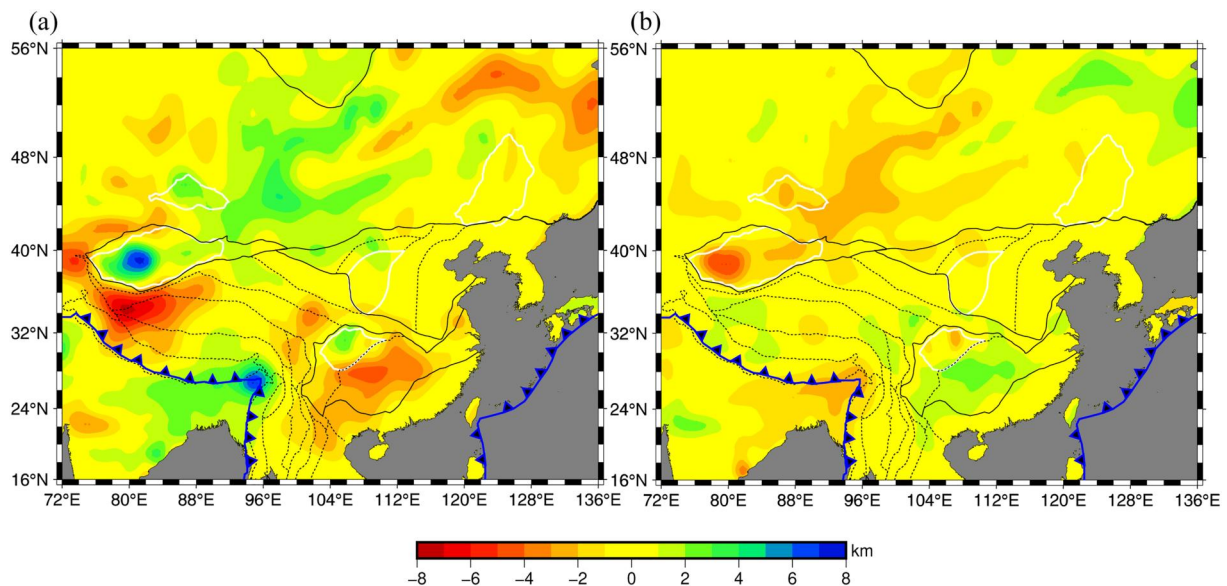


**Figure 11.** Differences between CPD results derived from various susceptibility models. (a) Model I: 0.01, 0.03, 0.07 SI in the upper, middle and lower crust and 0.001 SI in lithospheric mantle. (b) Model II: 0.01, 0.05, 0.09 SI in the upper, middle and lower crust and 0.001 SI in lithospheric mantle. Positive value indicates that the CPD is deeper than that shown in Figure 3.

established based on rock susceptibility measurement and crustal model. For the initial model, we chose a CPD based on 3D numerical thermal simulation. The Li-Oldenburg logarithmic barrier constrained inversion is adopted in the inversion process.

Our results show that the average CPD in the study area is slightly shallower than that of Moho, and the CPD is deep in stable and low heat flow areas and shallow in active tectonic regions. The surface heat flow is estimated by CPD based on 1D steady-state heat conduction equation, which is in good agreement with the measured heat flow. The comparison between CPD and Moho shows that CPD is much shallower than Moho in the Tibetan Plateau and CAOB, while slightly deeper than Moho in the Junggar Basin, Tarim Basin and Sichuan Basin. The differences between our model and two recent global models are mainly reflected in the Tarim Craton and Tibetan Plateau. The CPD obtained in this study is consistent with inferences of crustal thermal structure from heat flow, seismic velocity and magnetotelluric observations.

### Conflict of Interest

The authors declare no conflicts of interest relevant to this study.

### Data Availability Statement

The inversion code employed in this study is available at Lei and Jiao (2024) (<https://doi.org/10.5281/zenodo.10531967>). The figures were made with Generic Mapping Tools version 6 (Wessel et al., 2019). This continental Curie Point Depth model for China and surroundings and related data are available at Lei and Jiao (2024) (<https://doi.org/10.5281/zenodo.10531996>).

### Acknowledgments

This work was financially supported by grants from the Natural Science Foundation of China (42074072, U2239201) and the Special Fund of the Institute of Geophysics, China Earthquake Administration (DQJB22B23, DQJB23X15). We are grateful to Yujun Sun for providing the surficial radioactive heat production data. Constructive comments and suggestions by Prof. Douglas Schmitt (JGR AE), Prof. Jeff Gee (reviewer) and another anonymous reviewer helped greatly to improve the manuscript.

### References

- Alken, P., Thébault, E., Beggan, C. D., Amit, H., Aubert, J., Baerenzung, J., et al. (2021). International geomagnetic reference field: The thirteenth generation. *Earth Planets and Space*, 73(1), 49. <https://doi.org/10.1186/s40623-020-01288-x>
- Amante, C., & Eakins, B. W. (2009). ETOPO1 1 Arc-minute global relief model: Procedures, data source and analysis. NOAA technical memorandum NESDIS NGDC-24. *Nation Geophysical Data Center, NOAA*. <https://doi.org/10.7289/V5C8276M>
- An, M., Wiens, D. A., Zhao, Y., Feng, M., Nyblade, A., Kanao, M., et al. (2015). Temperature, lithosphere-asthenosphere boundary, and heat flux beneath the Antarctic Plate inferred from seismic velocities. *Journal of Geophysical Research: Solid Earth*, 120(12), 8720–8742. <https://doi.org/10.1002/2015JB011917>
- Asgharzadeh, M. F., von Frese, R. R. B., & Kim, H. R. (2008). Spherical prism magnetic effects by Gauss-Legendre quadrature integration. *Geophysical Journal International*, 173(1), 315–333. <https://doi.org/10.1111/j.1365-246X.2007.03692.x>
- Audet, P., & Gosselin, J. M. (2019). Curie depth estimation from magnetic anomaly data: A re-assessment using multitaper spectral and Bayesian inference. *Geophysical Journal International*, 218(1), 494–507. <https://doi.org/10.1093/gji/ggz166>
- Blakely, R. (1995). *Potential theory in gravity and magnetic applications*. Cambridge Univ. Press. <https://doi.org/10.1017/CBO9780511549816>
- Blakely, R., Brocher, T., & Wells, R. (2005). Subduction-zone magnetic anomalies and implications for hydrated forearc mantle. *Geology*, 33(6), 445–448. <https://doi.org/10.1130/G21447.1>
- Bouligand, C., Glen, J., & Blakely, R. (2009). Mapping Curie temperature depth in the western United States with a fractal model for crustal magnetization. *Journal of Geophysical Research*, 114(B11), B11104. <https://doi.org/10.1029/2009JB006494>
- Demarco, P. N., Prezzi, C., & Bettucci, L. S. (2020). Review of Curie point depth determination through different spectral method applied to magnetic data. *Geophysical Journal International*, 224(1), 17–39. <https://doi.org/10.1093/gji/ggaa361>
- Dunlop, D. J., & Özdemir, Ö., (2007). Magnetizations in rocks and minerals, in *Treatise on Geophysics*, 5.08, Editor(s): Gerald Schubert. Elsevier, 277–336.
- Dunlop, D. J., Özdemir, Ö., & Costanzo-Alvarez, V. (2010). Magnetic properties of rocks of the Kapuskasing uplift (Ontario, Canada) and origin of long-wavelength magnetic anomalies. *Geophysical Journal International*, 182(3), 645–658. <https://doi.org/10.1111/j.1365-246X.2010.04778.x>
- Dyment, J., & Arkani-Hamed, J. (1998). Contribution of lithospheric remanent magnetization to satellite magnetic anomalies over the world's oceans. *Journal of Geophysical Research: Solid Earth*, 103(B7), 15423–15441. <https://doi.org/10.1029/97JB03574>
- Ferré, E. C., Friedman, S. A., Matin-Hernández, F., Feinberg, J. M., Conder, J. A., & Lonov, D. A. (2013). The magnetism of mantle xenoliths and potential implications for sub-Moho magnetic sources. *Geophysical Research Letters*, 40(1), 105–110. <https://doi.org/10.1029/2012GL054100>
- Ferré, E. C., Kuppenko, I., Matin-Hernández, F., Ravat, D., & Sanchez-Valle, C. (2021). Magnetic sources in the Earth's mantle. *Nature Reviews Earth and Environment*, 2(1), 59–69. <https://doi.org/10.1038/s43017-020-00107-x>
- Fox-Maule, C., Purucker, M. E., & Olsen, N. (2009). Inferring magnetic crustal thickness and geothermal heat flux from crustal magnetic field models. Retrieved from [http://core2.gsfc.nasa.gov/research/purucker/foxmaule\\_dkc09-09\\_greenland.pdf](http://core2.gsfc.nasa.gov/research/purucker/foxmaule_dkc09-09_greenland.pdf)
- Fox-Maule, C., Purucker, M. E., Olsen, N., & Mosegaard, K. (2005). Heat flux anomalies in Antarctica revealed by satellite magnetic data. *Science*, 309(5733), 464–467. <https://doi.org/10.1126/science.1106888>
- Frost, B. R., & Shive, P. N. (1986). Magnetic mineralogy of the lower continental crust. *Journal of Geophysical Research: Solid Earth*, 91(B6), 6513–6521. <https://doi.org/10.1029/JB091iB06p06513>
- Gao, G., Kang, G., Li, G., & Bai, C. (2015). Crustal magnetic anomaly in the Ordos region and its tectonic implications. *Journal of Asian Earth Sciences*, 109, 63–73. <https://doi.org/10.1016/j.jseas.2015.04.033>
- Gao, G., Lu, Q., Wang, J., & Kang, G. (2021). Constraining crustal thickness and lithospheric thermal state beneath the northeastern Tibetan Plateau and adjacent regions from gravity, aeromagnetic, and heat flow data. *Journal of Asian Earth Sciences*, 212, 104743. <https://doi.org/10.1016/j.jseas.2021.104743>

- Gard, M., & Hasterok, D. (2021). A global Curie depth model utilizing the equivalent source magnetic dipole method. *Physics of the Earth and Planetary Interiors*, 313, 106672. <https://doi.org/10.1016/j.pepi.2021.106672>
- Haldar, S. K. (2020). *Introduction to mineralogy and petrology* (2nd ed., pp. P109–P143). Elsevier. <https://doi.org/10.1016/C2019-0-00625-5>
- Hasterok, D., Halpin, J. A., Collins, A. S., Hand, M., Kreemer, C., Gard, M. G., & Glorie, S. (2022). New maps of global geological provinces and tectonic plates. *Earth-Science Reviews*, 231, 104069. <https://doi.org/10.1016/j.earscirev.2022.104069>
- He, L. (2015). Thermal regime of the North China craton: Implication for craton destruction. *Earth-Science Reviews*, 140, 14–26. <https://doi.org/10.1016/j.earscirev.2014.10.011>
- Hemant, K., & Maus, S. (2005). Geological modeling of the new CHAMP magnetic anomaly maps using a geographical information system technique. *Journal of Geophysical Research: Solid Earth*, 110(B12), B12103. <https://doi.org/10.1029/2005JB003837>
- Hunt, C. P., Moskowit, B. M., & Banerjee, S. K. (1995). Magnetic properties of rocks and minerals. *Rock physics & phase relations: A handbook of physical constants*. (Vol. 3, pp. 189–204). American Geophysical Union. <https://doi.org/10.1029/RF003p0189>
- Jia, R., Zhao, D., & Wu, J. (2022). P-Wave anisotropic tomography of NE China: Insight into lithospheric deformation, mantle dynamics and intraplate volcanism. *Geophysical Journal International*, 229(2), 1372–1391. <https://doi.org/10.1093/gji/ggab516>
- Jiang, G., Hu, S., Shi, Y., Zhang, C., Wang, Z., & Hu, D. (2019). Terrestrial heat flow of continent China: Updated dataset and tectonic implications. *Tectonophysics*, 753, 36–48. <https://doi.org/10.1016/j.tecto.2019.01.006>
- Jiao, L., Chen, H., & Gao, M. (2013). Magnetic constraints on the spatial distribution of seismicity. *Earthquake Science*, 26(2), 125–136. <https://doi.org/10.1007/s11589-013-0022-3>
- Kang, G., Gao, G., Bai, C., Shao, D., & Feng, L. (2012). Characteristics of the crustal magnetic anomaly and regional tectonics in the Qinghai-Tibet Plateau and the adjacent areas. *Science China Earth Sciences*, 55(6), 1028–1036. <https://doi.org/10.1007/s11430-011-4323-x>
- Kiss, J., Szarka, L., & Prácsér, E. (2005). Second-order magnetic phase transition in the earth. *Geophysical Research Letters*, 32(24), L24310. <https://doi.org/10.1029/2005GL024199>
- Kupenko, I., Aprilis, G., Vasiukov, D. M., McCammon, C., Chariton, S., Cerantola, V., et al. (2019). Magnetism in cold subducting slabs at mantle transition zone depths. *Nature*, 570(7759), 102–106. <https://doi.org/10.1038/s41586-019-1254-8>
- Laske, G., Masters, G., Ma, Z., & Pasyanos, M. (2013). Update on Crust1.0 - a 1-degree global model of earth's crust. *Geophysical Research Abstracts*, 15. Abstract EGU2013-2658 <http://igppweb.ucsd.edu/~gabi/rem.html>
- Lei, Y., & Jiao, L. (2024). Codes for CPD inversion (1.1) [Software]. *Zenodo*. <https://doi.org/10.5281/zenodo.10531967>
- Lei, Y., & Jiao, L. (2024). CPD model and data for CPD inversion (1.1) [Dataset]. *Zenodo*. <https://doi.org/10.5281/zenodo.10531996>
- Lei, Y., Jiao, L., & Chen, H. (2018). Possible correlation between the vertical component of lithospheric magnetic field and continental seismicity. *Earth, Planets and Space*, 70(1), 179. <https://doi.org/10.1186/s40623-018-0949-7>
- Li, C., Lu, Y., & Wang, J. (2017). A global reference model of Curie-point depths based on EMAG2. *Scientific Reports*, 7(1), 45129. <https://doi.org/10.1038/srep45129>
- Li, C., Wang, J., Lin, J., & Wang, T. (2013). Thermal evolution of the North Atlantic lithosphere: New constraints from magnetic anomaly inversion with a fractal magnetization model. *Geochemistry, Geophysics, Geosystems*, 14(12), 5078–5105. <https://doi.org/10.1002/2013GC004896>
- Li, H., Li, S., Song, X. D., Gong, M., Li, X., & Jia, J. (2012). Crustal and uppermost mantle velocity structure beneath northwestern China from seismic ambient noise tomography. *Geophysical Journal International*, 188(1), 131–143. <https://doi.org/10.1111/j.1365-246X.2011.05205.x>
- Li, X., Zhu, P., Kusky, T. M., Gu, Y., Peng, S., Yuan, Y., & Fu, J. (2015). Has the Yangtze craton lost its root? A comparison between the North China and Yangtze cratons. *Tectonophysics*, 655, 1–14. <https://doi.org/10.1016/j.tecto.2015.04.008>
- Li, Y., & Oldenburg, D. W. (1996). 3-D inversion of magnetic data. *Geophysics*, 61(2), 396–408. <https://doi.org/10.1190/1.1443968>
- Li, Y., & Oldenburg, D. W. (2003). Fast inversion of large-scale magnetic data using wavelet transforms and a logarithmic barrier method. *Geophysical Journal International*, 152(2), 251–265. <https://doi.org/10.1046/j.1365-246x.2003.01766.x>
- Lin, J. Y., Sibuet, J. C., & Hsu, S. K. (2005). Distribution of the East China Sea continental shelf basins and depths of magnetic sources. *Earth Planets and Space*, 57(11), 1063–1072. <https://doi.org/10.1186/BF03351885>
- Masterton, S. M., Gubbins, D., Müller, R. D., & Singh, K. H. (2013). Forward modelling of oceanic lithospheric magnetization. *Geophysical Journal International*, 192(3), 951–962. <https://doi.org/10.1093/gji/ggs063>
- Maus, S., Barckhaysen, U., Berkenbosch, H., Bournas, N., Brozena, J., Childers, V., et al. (2009). EMAG2: A 2-arc min resolution earth magnetic anomaly grid compiled from satellite, airborne, and marine magnetic measurements. *Geochemistry, Geophysics, Geosystems*, 10(8). <https://doi.org/10.1029/2009GC002471>
- Maus, S., & Haak, V. (2002). Is the long wavelength crustal magnetic field dominated by induced or by remanent magnetization? *Journal Indian Geophysical Union*, 6(1), 1–5. [https://gfzpublic.gfz-potsdam.de/rest/items/item\\_230994\\_1/component/file\\_230993/content](https://gfzpublic.gfz-potsdam.de/rest/items/item_230994_1/component/file_230993/content)
- McEnroe, S. A., Robinson, P., Chruch, N., & Purucker, M. (2017). Magnetism at depth: A view from an ancient continental subduction and collision zone. *Geochemistry, Geophysics, Geosystems*, 19(4), 1123–1147. <https://doi.org/10.1002/2017GC007344>
- Olsen, N., Ravat, D., & Purucker, M. E. (2023). One the determination and interpretation of the lithospheric induced magnetization. *Earth and Planetary Science Letters*, 606, 118038. <https://doi.org/10.1016/j.epsl.2023.118038>
- Purucker, M. E., & Dyment, J. (2000). Satellite magnetic anomalies related to seafloor spreading in the South Atlantic Ocean. *Geophysical Research Letters*, 27(17), 2765–2768. <https://doi.org/10.1029/1999GL008437>
- Purucker, M. E., Langlais, B., Olsen, N., Hulot, G., & Manda, M. (2002). The southern edge of cratonic north America: Evidence from new satellite magnetometer observations. *Geophysical Research Letters*, 29(15), 1–4. <https://doi.org/10.1029/2001GL013645>
- Rajaram, M., Anand, S. P., Hemant, K., & Purucker, M. E. (2009). Curie isotherm map of Indian subcontinent from satellite and aeromagnetic data. *Earth and Planetary Science Letters*, 281(3), 147–158. <https://doi.org/10.1016/j.epsl.2009.02.013>
- Rippe, D., & Unsworth, M. (2010). Quantifying crustal flow in Tibet with magnetotelluric data. *Physics of the Earth and Planetary Interiors*, 179(3–4), 107–121. <https://doi.org/10.1016/j.pepi.2010.01.009>
- Salem, A., Green, C., Ravat, D., Singh, K., East, P., Fairhead, J., et al. (2014). Depth to Curie temperature across the central Red Sea from magnetic data using the de-fractal method. *Tectonophysics*, 624–625, 75–86. <https://doi.org/10.1016/j.tecto.2014.04.027>
- Sen, G. (2014). *Petrology* (pp. P19–P49). Springer Berlin. <https://doi.org/10.1007/978-3-642-38800-2>
- Shive, P. N. (1989). Can remanent magnetization in the deep crust contribute to long wavelength magnetic anomalies? *Geophysical Research Letters*, 16(1), 89–92. <https://doi.org/10.1029/GL016i001p00089>
- Sun, S., Du, J., Zhi, J., Chen, C., & Xu, H. (2022). A constrained approach by Curie point depth estimation for the 3-D inversion of regional lithospheric magnetic anomaly data in spherical coordinates and its application to the Northern Xinjiang, China. *Journal of Geophysical Research: Solid Earth*, 127(8), e2021JB023149. <https://doi.org/10.1029/2021JB023149>
- Sun, Y., Dong, S., Wang, X., Liu, M., Zhang, H., & Shi, Y. (2022). Three-Dimensional thermal structure of east Asian continental lithosphere. *Journal of Geophysical Research: Solid Earth*, 127(5), e2021JB023432. <https://doi.org/10.1029/2021JB023432>

- Sven, F., & Ben, N. (2021). *International heat flow commission: The global heat flow Database: Release 2021*. GFZ Data Services. <https://doi.org/10.5880/idgeo.2021.014>
- Szwillus, W., Baykiev, E., Dilixiati, Y., & Ebbing, J. (2022). Linearized Bayesian estimation of magnetization and depth to magnetic bottom from satellite data. *Geophysical Journal International*, 230(3), 1508–1533. <https://doi.org/10.1093/gji/ggac133>
- Tan, P., Liang, X., Li, W., & Wu, C. (2023). Crustal structure of the Tibetan Plateau and adjacent areas revealed from ambient noise tomography. *Gondwana Research*, 121, 1–15. <https://doi.org/10.1016/j.gr.2023.03.029>
- Tanaka, A., Okubo, Y., & Matsubayashi, O. (1999). Curie point depth based on spectrum analysis of the magnetic anomaly data in East and Southeast Asia. *Tectonophysics*, 306(3–4), 461–470. [https://doi.org/10.1016/S0040-1951\(99\)00072-4](https://doi.org/10.1016/S0040-1951(99)00072-4)
- Thébault, E., Purucker, M. E., Whaler, K. A., Langlais, B., & Sabaka, T. J. (2010). The magnetic field of the earth's lithosphere. *Space Science Reviews*, 155(1–4), 95–127. <https://doi.org/10.1007/s11214-010-9667-6>
- Wang, J., & Li, C. (2018). Curie point depths in Northeast China and their geothermal implications for the Songliao Basin. *Journal of Asian Earth Sciences*, 163, 177–193. <https://doi.org/10.1016/j.jseas.2018.05.026>
- Wasilewski, P. J., & Mayhew, M. A. (1992). The moho as a magnetic boundary revisited. *Geophysical Research Letters*, 19(22), 2259–2262. <https://doi.org/10.1029/92GL01997>
- Wessel, P., Luis, J. F., Uieda, L., Scharroo, R., Wobbe, F., Smith, W. H. F., & Tian, D. (2019). The generic mapping Tools version 6 [Software]. *Geochemistry, Geophysics, Geosystems*, 20(11), 5556–5564. <https://doi.org/10.1029/2019GC008515>
- Williams, S. E., & Gubbins, D. (2019). Origin of long-wavelength magnetic anomalies at subduction zones. *Journal of Geophysical Research: Solid Earth*, 124(9), 9457–9473. <https://doi.org/10.1029/2019JB017479>
- Xiong, S., Yang, H., Ding, Y., & Li, Z. (2016). Characteristics of Chinese continent Curie point isotherm. *Chinese Journal of Geophysics*, 59(10), 3604–3617. <https://doi.org/10.6038/cjg20161008>
- Xiong, S., Yang, H., Ding, Y., Li, Z., & Li, W. (2016). Distribution of igneous rocks in China revealed by aeromagnetic data. *Journal of Asian Earth Sciences*, 129, 231–242. <https://doi.org/10.1016/j.jseas.2016.08.016>
- Xu, X., Xiong, S., Tanaka, A., Zheng, Q., Kuang, X., Zhu, X., et al. (2021). Thermal structure beneath the Tarim craton and its tectonic implications. *Frontiers in Earth Science*, 9, 700114. <https://doi.org/10.3389/feart.2021.700114>
- Zhang, X., Wang, Q., Wyman, D., Kerr, A. C., Dan, W., & Qi, Y. (2022). Tibetan Plateau insights into > 1100°C crustal melting in the Quaternary. *Geology*, 50(12), 1432–1437. <https://doi.org/10.1130/G50387.1>
- Zhu, R., Xu, Y., Zhu, G., Zhang, H., Xia, Q., & Zheng, T. (2012). Destruction of the North China craton. *Science China Earth Sciences*, 55(10), 1565–1587. <https://doi.org/10.1007/s11430-012-4516-y>